PHYSICAL REVIEW B **86**, 064203 (2012)

Coexistence of long- and short-range magnetic order in the frustrated magnet $SrYb_2O_4$

D. L. Quintero-Castro,[1,2,*] B. Lake,[1,2] M. Reehuis,[1] A. Niazi,[3] H. Ryll,[1,2] A. T. M. N. Islam,[1] T. Fennell,[4,5] S. A. J. Kimber,[1,6] B. Klemke,[1] J. Ollivier,[4] V. Garcia Sakai,[7] P. P. Deen,[4,8] and H. Mutka[4]

[1]*Helmholtz-Zentrum Berlin für Materialien und Energie, D-14109 Berlin, Germany*

[2]*Institut für Festkörperphysik, Technische Universität Berlin, D-10623 Berlin, Germany*

[3]*Department of Physics, Faculty of Natural Sciences, Jamia Millia Islamia University, New Delhi 110025, India*

[4]*Institut Laue Langevin, 6 rue Jules Horowitz, BP 156, F-38042, Grenoble Cedex 9, France*

[5]*Laboratory for Neutron Scattering, PSI, CH-5232 Villigen, Switzerland*

[6]*ESRF, 6 Rue Jules Horowitz BP 220, F-38043 Grenoble Cedex 9, France*

[7]*ISIS Pulsed Source, Rutherford Appleton Laboratory, Chilton, Didcot, United Kingdom*

[8]*European Spallation Source ESS AB, P.O. Box 176, SE-22100 Lund, Sweden*

(Received 29 May 2012; published 13 August 2012)

$SrYb_2O_4$ is a geometrically frustrated rare-earth magnet, which presents a variety of interrelated magnetic phenomena. The magnetic Yb^{3+} ions ($J = 7/2$) form potentially frustrated "zigzag" chains along the c axis, arranged in a honeycomb fashion in the ab plane. Heat capacity reveals a magnetic phase transition at $T_N = 0.9$ K. The magnetic structure was solved by polarized neutron diffraction and found to be noncollinear with a reduction of the ordered spin moment from the full ionic moment. The low-energy excitations, which were measured by inelastic neutron scattering reveal diffuse scattering both above and below T_N. Heat capacity and magnetocaloric effect were performed to map out the magnetic phase diagram as a function of magnetic field and temperature and show a complicated series of states. Altogether, the results suggest that the magnetic interactions in $SrYb_2O_4$ compete with each other and with the single-ion anisotropy to produce a highly degenerate ground state manifold that suppresses the magnetic order, broadens the excitations and gives rise to a complex phase diagram.

DOI: 10.1103/PhysRevB.86.064203 PACS number(s): 61.05.fg, 75.25.−j, 75.47.Lx, 75.50.Ee

I. INTRODUCTION

Frustrated magnetism is a topic in condensed matter physics that is currently under intense investigation. In geometrically frustrated magnets, the arrangement of magnetic ions (e.g., triangular or tetrahedral) prevents the simultaneous minimization of energy on all magnetic bonds if the interactions between the magnetic ions are antiferromagnetic. The cases that are usually investigated contain transition metal ($3d$) ions with orbital angular momentum that is mostly quenched and thus the single ion anisotropy is negligible or small. On the other hand, when the magnetic ion is a rare earth ($4f$) the angular momentum is unquenched resulting in strong single ion anisotropy, which in some cases can compete with the interactions between the magnetic ions.[1] For example, it may favor particular magnetic moment directions that are incompatible with the magnetic structure preferred by the interactions. Another feature of rare-earth magnets is that dipolar interactions between nearest neighbors can be strong, in some cases larger than the exchange interactions due to the large size of the magnetic moments.[2,3] Together these features give rise to a large number of potentially unusual magnetic states, such as spin ice, spin liquids, co-operative paramagnetism, and partially ordered states in which long- and short-range magnetic correlations coexist.[4–6]

Some examples are the rare-earth pyrochlores, $R_2M_2O_7$ (R = rare-earth atom, M = Ti, Sn, Zr).[7] It has been shown that it is the competition between the dipolar interactions and the Ising anisotropy that causes the spin ice phenomenology in $Dy_2Ti_2O_7$ and $Ho_2Ti_2O_7$.[8,9] In $Er_2Ti_2O_7$ where the anisotropy is planar (xy-type), long-range magnetic order is stabilized from the ground-state manifold via an order-by-disorder mechanism.[10–12] $Tb_2Ti_2O_7$ is a co-operative paramagnet that fails to develop long-range order down to 0.05 K, in this material, dipolar interactions play a very important role in frustrating the nearest-neighbor exchange interactions.[13,14] Another example of a frustrated rare-earth insulator is $Gd_3Ga_5O_{12}$ which consists of corner sharing triangles. Although antiferromagnetic interactions are present it does not order down to 0.025 K and there is experimental evidence for a spin-liquid ground state. This compound does however develop long-range magnetic order in an applied magnetic field.[15,16]

Recently, interest has grown in a new family of insulating frustrated rare-earth antiferromagnets SrR_2O_4.[17–19] The nuclear structure of these compounds consists of zigzag chains running along the c axis, where the similar first- and second-neighbor distances suggests the possibility of competing first- and second-neighbor exchange interactions. In the ab plane, the ions form a honeycomb structure, which is characterized by a low coordination number. These features are well known to enhance quantum fluctuations and in combination with a strong single-ion anisotropy suppress long-range order, in spite of the three-dimensional (3D) nature of the magnetic interactions. The competition between the single-ion anisotropy and frustrated magnetic interactions is reflected by a reduced Néel temperature or complete suppression of magnetic order. However, the magnetic properties of most of these compounds have not been investigated in detail until now.

Magnetic susceptibility and powder neutron diffraction of SrR_2O_4 with R = Dy, Ho, Tm, and Yb were published by Karunadasa *et al.* (see Ref. 17). $SrDy_2O_4$ shows magnetic scattering at low temperatures (below 5 K) due to short-range correlations, however, no long-range magnetically ordered

phase has been detected down to 20 mK.[19] In contrast, the Ho compound exhibits long-range two dimensional order. $SrEr_2O_4$ has been investigated in detail by Petrenko *et al.*[18] They report long range AFM order below $T = 0.75$ K, but where the ordered moment is substantially reduced from the full ionic moment. The excitations show a combination of sharp magnon-type features alongside diffuse scattering.

Interesting magnetic phenomena are also expected in $SrYb_2O_4$. In this compound, the magnetic Yb^{3+} ion is characterized by an angular momentum $S = 1/2$, $L = 3$, $J = 7/2$, and a Landé factor $g = 8/7$. The effect of an orthorhombic crystal field on the ion is to lift the degeneracy of the ground state manifold into four doublets according to Kramer's theorem. Karunadasa *et al.* (see Ref. 17) did not find any magnetic transition down to 2 K in this material, although the presence of short-range magnetic correlations at low temperatures was suggested based on susceptibility measurements.

We have grown the first large single crystal of $SrYb_2O_4$, which provide the opportunity to thoroughly investigate the magnetic properties of this compound. This paper describes the nuclear and magnetic structure determination of $SrYb_2O_4$ using neutron diffraction, along with an exploration of the low energy magnetic excitations using inelastic neutron scattering and construction of the magnetic phase diagram using heat capacity and magnetocaloric effect measurements.

The results reveal that $SrYb_2O_4$ develops long-range magnetic order below $T_N = 0.9$ K but with a reduction in the ordered moment compared to the ionic moment. The magnetic excitations within the ground-state doublet show coexistence of sharp and diffuse features suggesting the presence of competing interactions. This is further confirmed by the magnetic phase diagram that reveals a series of metamagnetic transitions. Altogether, the results reveal rich and complex magnetic properties characterized by the competition between single-ion anisotropy and exchange interactions.

II. EXPERIMENTAL DETAILS

Powder samples of $SrYb_2O_4$ were synthesized by a solid state reaction. Stoichiometric amounts of $SrCO_3$ (99.994% purity, Alfa Aesar) and Yb_2O_3 (99.97% purity, Alfa Aesar) were mixed thoroughly, pressed into a pellet and heated three times for periods of 38 hours at 1400–1550 °C with intermediate grindings to achieve a single phase powder of $SrYb_2O_4$. Single crystals were grown from the melt by the floating zone technique using a high-temperature optical floating zone furnace (Crystal Systems Inc. Model FZ-T−10000−H-VI-VPO). For this, the powder was pressed into a feed rod using a cold isostatic press (EPSI). The floating zone furnace was used to melt the tip of the feed rod, which recrystallized on a seed crystal to achieve single-phase growth, the molten zone was then moved along the feed rod at a rate of 1 mm/hour to obtain a large single crystal. The growth was performed in air at ambient pressure. The resulting samples were typically transparent and cylindrical with a diameter of ≈5 mm and length of 20 mm.

In order to study the nuclear structure of $SrYb_2O_4$, the fine resolution powder diffractometer E9 at the BER II reactor at the Helmholtz-Zentrum Berlin (HZB) was used. An incident neutron wavelength of 1.798 Å was selected by a Ge(511) monochromator. A hollow cylindrical Cu sample can was filled with 6 g of $SrYb_2O_4$ powder. A mixture of deuterated ethanol and methanol was added to ensure thermal contact, the can was then attached to a dilution insert. Data were collected at two temperatures $T = 0.03$ and 10 K, with a counting time of 72 hours each.

In addition, the D7 diffractometer at the Institut Laue-Langevin (ILL), which can perform **XYZ** polarization analysis, was used to measure both powder patterns and single crystal Bragg reflections of $SrYb_2O_4$.[20] For both measurements, the samples were cooled in a dilution fridge to a minimum temperature of $T = 0.03$ K, the incident wavelength was $\lambda_0 = 4.84$ Å. In the case of the powder measurements, the 11-g sample was used, in an annular Cu can. Six polarization channels were measured at $T = 29$ mK, $\mathbf{XX}_{\mathrm{nsf}}$, $\mathbf{YY}_{\mathrm{nsf}}$, $\mathbf{ZZ}_{\mathrm{nsf}}$, $\mathbf{XX'}_{\mathrm{sf}}$, $\mathbf{YY'}_{\mathrm{sf}}$ and $\mathbf{ZZ'}_{\mathrm{sf}}$ (where the subscripts "nsf" and "sf" refer to the non-spin-flip and spin-flip channels), while scanning the 2θ angle of the detectors. The procedure was repeated for 36 hours to acquire good statistics. Calibrations using amorphous silica, vanadium, and empty can were performed.

For the single crystal measurements, a single crystal of 3.2-g weight was mounted on a Cu holder with $(H,K,0)$ as the scattering plane. We measured 11 Bragg peaks at 0.03 K, each with six different polarizations. For these measurements, five different detector positions were used around the nominal 2θ for each Bragg peak, and for each of these positions ω scans of 30° (step size 0.15°) were performed and counted for eight seconds at every position and polarization channel.[20–22]

Single-crystal inelastic neutron scattering was performed using the Time-of-Flight (ToF) IN5 spectrometer, at the ILL. A single crystal of 3.2 g was mounted on a copper sample stick and inserted inside a dilution fridge in order to reach low temperatures. The $(0,K,L)$ plane was in the horizontal scattering plane and data were collected along all directions (H,K,L) using the position-sensitive detectors. The crystal was rotated about a vertical axis and a range of 100° was scanned in 1° steps. The spectrum was measured at each angle for 40 min (370 000 monitor counts) at a base temperature of $T = 0.06$ K and initial wavelength of $\lambda_0 = 5.5$ Å (2.70 meV), the resolution at the elastic line was 62 μeV. Higher-temperature scans were done in a similar way for wavelengths of 5 Å (3.27 meV), with resolution at the elastic line of 90 μeV and 3 Å (9.09 meV), giving a resolution of 260 μeV. Data sets at $T = 1.6$, 2, 20, and 40 K were acquired. The data were combined using the HORACE software (see Ref. 23) to make a 4D data set as a function of H,K,L,E.

Single-crystal neutron scattering was also performed using the IRIS indirect geometry chopper spectrometer at ISIS. The same single crystal used for the measurement on IN5 was aligned with $(H,K,0)$ in the horizontal scattering plane. The crystal was rotated about a vertical axis over a range of 98° with 2° steps and for some regions 1° steps. The spectrum was measured at each angle for 300 μAmps using a fixed final energy of 1.845 meV (6.66 Å), which provided energy transfers up to 1.9 meV. All spectra were measured in the AFM ordered phase at 50 mK. To reach this temperature, a dilution fridge was used. These data sets were also recombined using the HORACE software.

The dc magnetic susceptibility was measured using a Quantum Design Physical Property Measurement System (PPMS) with a Vibrating Sample Magnetometer (see Ref. 24) at the Laboratory for Magnetic Measurements, HZB. The single crystal was oriented using the x-ray Laue technique, cut and installed in a brass sample holder. The susceptibility was measured along all main crystallographic directions by applying a 1-T field and sweeping temperature from 2–970 K. The magnetization was also measured at 2 K for magnetic fields from 0 to 14 T applied along the three different crystallographic directions.

Heat capacity and magnetocaloric effect (MCE) measurements on single-crystal samples were performed to map out the magnetic phase diagram of $SrYb_2O_4$. These measurements were done using a homemade calorimeter at HZB. The oriented samples were mounted on a sapphire calorimeter chip, which is thermally coupled to the thermal bath. Temperature and magnetic field control were provided by a Heliox type ^{3}He sorption cryostat inserted in a 14.5-T cryomagnet.[25] The samples used were a single crystal piece of 3.07 mg oriented along the a and c axes as well as a 1.87-mg single crystal aligned along the b axis. The heat capacity was measured in the temperature range 0.28 K $< T <$ 1.1 K for the samples aligned along the a and b axes and 0.28 K $< T <$ 9 K for the sample aligned along the c axis. Constant magnetic fields up to 12 T were applied along the three crystallographic axes. For the heat capacity measurements above 10 K, the PPMS was used.

The magnetocaloric effect (MCE) was also measured on the homemade calorimeter at constant temperatures from 0.3 to 1 K, the magnetic field was applied along the a, b, and c axes and was ramped up and down from 0 to 12 T with a sweep rate of 0.075 T/min.

III. RESULTS

A. Nuclear structure

The powder neutron diffraction patterns acquired on E9 both well above and below the Néel temperature ($T_N = 0.9$ K) are shown in Fig. 1. The patterns were fitted using the Rietveld method in FULLPROF.[26] The diffraction pattern contained a few Cu Bragg peaks from the Cu sample can, which were excluded during the refinements. The crystal structure could be refined successfully in the space group $Pnam$ (No. 62) used previously by other groups.[17,27–30] An excellent refinement was achieved resulting in a residual of the refinement $R_N = 0.0248$, thus confirming an orthorhombic structure with space group $Pnam$. The resulting lattice parameters and atomic positions at $T = 10$ K are listed in Table I. The low-temperature ($T = 40$ mK) E9 powder diffraction pattern was also refined. The crystal and magnetic structure (explained in Sec. III C) were fitted simultaneously and reveal no significant structural change accompanying the magnetic transition, these results are also listed in Table I.

The nuclear structure of $SrYb_2O_4$ consists of nonmagnetic Sr^{2+} ions filling the columnar cavities of a network of edge and corner shared YbO_6 octahedra. These octahedra form a honeycomb-like structure in the ab plane, see Fig. 2. The Yb^{3+} ions are arranged in zigzag chains running parallel to the c axis. Each chain contains only one of the two crystallographically

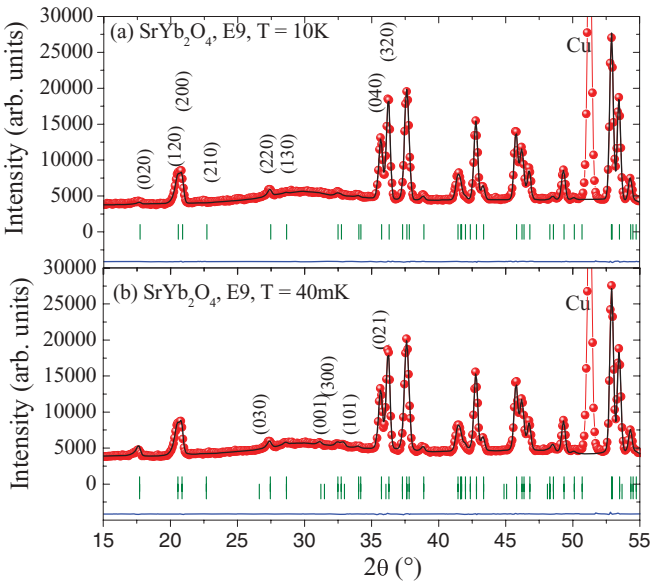

FIG. 1. (Color online) Observed, calculated, and difference profiles from the Rietveld refinement of the E9 data collected at (a) $T = 10$ K and (b) $T = 40$ mK. The copper reflections were excluded during the refinements. The calculated patterns (black lines) are compared with the observed ones (red dots). The blue line represents the difference between them and the green bars indicate the (h,k,l) positions.

independent Yb^{3+} ions. All atoms are on the $4c(x,y,1/4)$ Wyckoff position. The YbO_6 octahedra are distorted, with only mirror plane symmetry. Since the Yb^{3+}-Yb^{3+} distances are short (see Fig. 2), we can expect magnetic interactions between them giving rise to long-range magnetic order.

B. Direct current magnetic susceptibility, heat capacity, and magnetic entropy

Figure 3 shows the inverse static susceptibility of $SrYb_2O_4$ with a magnetic field applied along the three different crystallographic axes over the temperature range –970 K. There is a marked difference well above the Néel temperature between the susceptibility with a magnetic field

TABLE I. Crystal structure parameters of $SrYb_2O_4$ from the refinement of the E9 data at $T = 40$ mK and $T = 10$ K. All the atoms are located on the Wyckoff site $4c(x,y,1/4)$ of the space group $Pnam$. The lattice parameters at 40 mK are $a = 9.97576(7)$ Å, $b = 11.75466(8)$ Å, and $c = 3.35260(3)$ Å and at 10 K, they are $a = 9.97595(7)$ Å, $b = 11.75488(7)$ Å, and $c = 3.35265(2)$ Å.

	$SrYb_2O_4$ at 40 mK		$SrYb_2O_4$ at 10 K	
Atom	x	y	x	y
Sr	0.7546(3)	0.6512(3)	0.7544(3)	0.6514(3)
Yb1	0.4217(2)	0.1090(1)	0.4221(2)	0.1091(1)
Yb2	0.4264(2)	0.6123(2)	0.4260(2)	0.6124(2)
O1	0.2108(4)	0.1725(3)	0.2106(4)	0.1736(3)
O2	0.1246(4)	0.4800(3)	0.1236(4)	0.4798(4)
O3	0.5179(4)	0.7833(3)	0.5183(4)	0.7835(3)
O4	0.4219(4)	0.4229(3)	0.4217(5)	0.4230(3)

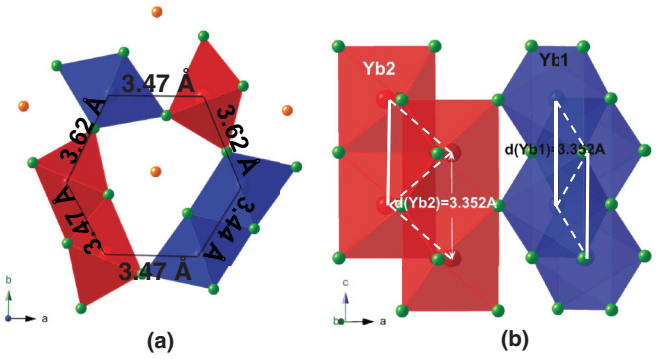

FIG. 2. (Color online) Crystal structure of $SrYb_2O_4$ projected onto the (a) *ab* and (b) *ac* planes. The O^{2-} are represented by green circles. The Yb^{3+} cations lie inside the octahedra, Yb1 in the blue octahedra and Yb2 in the red octahedra. Sr^{2+} ions are in orange and are only shown in (a). The Yb^{3+}-Yb^{3+} distances are obtained from the E9 refinement at $T = 10$ K.

applied along the *c* axis compared to the *a* and *b* axes, suggesting significant magnetic anisotropy. The *c* axis is a unique axis for both Yb1 and Yb2 since it lies perpendicular to the mirror plane which characterizes both Yb sites. In contrast, the *a* and *b* axes do not correspond to unique anisotropy directions which are in any case different for the two Yb^{3+} ions within the *ab* plane. The results were fitted to the Curie-Weiss law, the fits are shown in the figure as black lines and the fitted parameters are listed in Table II. The results indicate Curie-like behavior above $T = 700$ K. The Curie-Weiss temperatures are in agreement with the value of -99.4 K obtained by Karunadasa *et al.* for a powder sample.[17]

The effective moment calculated from the fit of the magnetic static susceptibility is $4.31\mu_B$, which is slightly reduced from the theoretical value of $4.54\mu_B$. This is probably because the four doubly degenerate levels of the $J = 7/2$ multiplet, which are split by the octahedral crystal field, are not fully populated even at 1000 K so that the full moment is not achieved. Furthermore, in the low-temperature region there is a gradual change in slope that suggests an onset of short-range order [see Fig. 3(inset)].

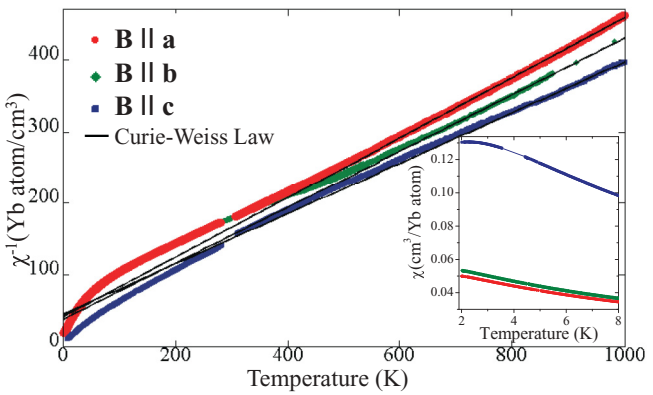

FIG. 3. (Color online) Inverse dc susceptibility measured with an applied magnetic field of 1 T along the three principle crystallographic directions, the three black solid lines represent the fit to the Curie-Weiss law for each direction. (Inset) Low-temperature dc susceptibility.

TABLE II. Results of the fit of the high temperature inverse susceptibility (temperature range 700–970 K) to the Curie-Weiss law. For all fits, the correlation coefficient was over 0.99.

B ||	$\theta(K)$	C(cm^3K/mol)	μ_{eff} (μ_B)
a	−98(1)	2.396(3)	4.17
b	−96(1)	2.550(4)	4.30
c	−127(2)	2.841(6)	4.50

The heat capacity of $SrYb_2O_4$ is shown in Fig. 4. At low temperatures, two anomalies were found, a lambdalike transition at 0.92 K related to an onset of long-range AFM order and a Schottky-type peak at 2.5 K related to short range magnetic correlations. The entropy per formula unit mole (2 Yb^{3+} ions) was calculated and was found to sum up to $2R\ln 2$ (at ≈10 K), suggesting the presence of a doublet ground state as expected for a Kramer's ion and no excited state below 10 K (0.86 meV). The inset in Fig. 4 shows the heat capacity of $SrYb_2O_4$ for different magnetic fields applied along the *c* axis. The lambdalike peak shifts towards lower temperatures when applying a magnetic field; whereas the Schottky-type peak initially decreases and moves towards higher temperatures with increasing field. A change occurs above $B = 4$ T where the shoulder broadens and its heat capacity increases.

C. Magnetic structure

The heat capacity reveals that $SrYb_2O_4$ undergoes a phase transition to long-range magnetic order around $T = 0.92$ K in zero field. The comparison between the high- and low-temperature powder-diffraction patterns recorded on E9, shows additional magnetic intensities at the positions of nuclear Bragg peaks as well as at the positions of the peaks

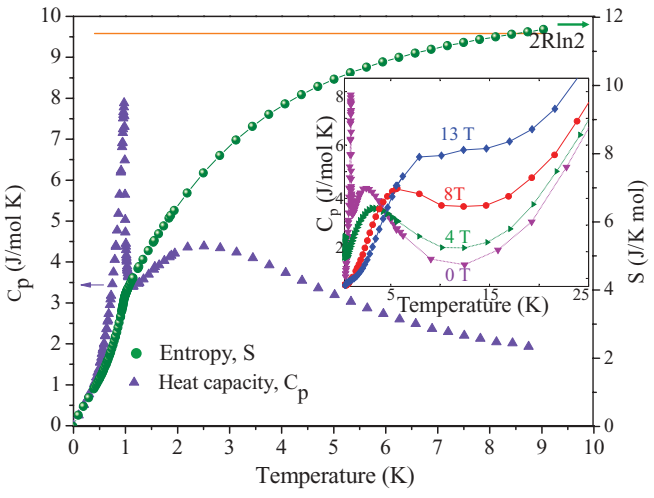

FIG. 4. (Color online) Heat capacity and magnetic entropy for $SrYb_2O_4$. Purple points are low-temperature zero-field heat capacity and green points are the total entropy. The entropy sums up to $2R\ln 2$ per two Yb^{2+} ions (orange line) at 10 K, suggesting that there are no excited CF levels at low energies (below 0.9 meV). (Inset) Heat capacity for different magnetic fields applied along the *c* axis. Below a temperature of 13 K, the phonon contribution is negligibly small when compared to the magnetic contribution.

(0,0,1) and (1,0,1), which are forbidden for the space group $Pnam$. Due to the fact that the nuclear and the magnetic unit cells are the same, the magnetic structure can be described with the propagation vector $k = (0,0,0)$. In order to separate the nuclear and magnetic components, polarization analysis was used. Using the D7 instrument, **XYZ** polarization analysis was performed to measure the powder diffraction pattern of $SrYb_2O_4$ in the antiferromagnetic phase as well as some selected single-crystal Bragg peaks in the antiferromagnetic phase. The integrated intensities of these peaks for all polarization channels are listed in Table V of Appendix.

Inspection of the peak intensities in the different polarization channels provides a lot of information. The most important information is given by the spin-flip components, which do not contain any nuclear intensity, but are purely magnetic and spin incoherent. Thus it is possible to identify whether a reflection is entirely nuclear or magnetic or a mixture. The **X** and **Y** polarization directions lie in the horizontal scattering plane but do not coincide with the crystal axes. (It should be noted that the **X**,**Y**, **Z** coordinate system for the polarization is different from a, b, c or x, y, z coordinate system of the crystal.) The **Z** polarization direction is vertical and can provide particularly important information. By orienting the $SrYb_2O_4$ crystal so that the c axis coincides with the vertical **Z** axis of the polarization, only magnetic components along the c axis are observed in the *sf* channel of the **Z** polarization.

In order to find the magnetic structure that is compatible with the space group symmetry, we performed representation analysis.[31] There are two different Yb^{3+} sites (both at the Wyckoff positions 4c) each of which generates four Yb^{3+} ions in the unit cell at fractional coordinates $(x,y,1/4)$, $(-x,-y,3/4)$ and $(x+1/2,-y+1/2,1/4)$, $(-x+1/2,y+1/2,3/4)$. Using the BASIREPS program in the FULLPROF suite (see Ref. 26), the allowed relative ordering patterns for this sequence of Yb^{3+} ions were determined for the possible representations. Furthermore, the relative intensities expected for these patterns were simulated, see Table IV in Appendix. By comparing the simulated intensities with the measured Bragg peak intensities in the different polarization channels (see Table V) the magnetic structure was deduced (see Appendix for full details). The results show that $SrYb_2O_4$ follows the A_x and G_y modes corresponding to relative orders of $(+--+)$ along the a direction and $(+--+)$ along the b direction for the four equivalent Yb^{3+} ions listed above. The magnetic moments lie mostly in the ab plane, and the two inequivalent Yb^{3+} ions have different sized ordered moments (see Appendix for comparison of the two cases, first when the two sites have different ordered moments and second when they have same sized ordered moment).

Using these results, the magnetic component of the powder pattern acquired on D7 was refined. To achieve this, the magnetic, nuclear, and incoherent components of the polarized powder diffraction data acquired at 30 mK were separated using the approach described by Stewart *et al.*[20] The Schärpf angle was set to $\alpha = 90^\circ$, this is valid for systems where the magnetic order has a zero net component, such as an antiferromagnet or a paramagnet. The nuclear component was refined with the fixed atomic positions and lattice parameters fixed to the values obtained from the refinement of the E9 powder data. The magnetic component was refined

TABLE III. Results of the magnetic structure refinement assuming $\Gamma_4(A_xG_y)$ ($\mu_z = 0$) of the magnetic component of the D7 diffraction pattern. Profile residual $R_p = 0.0353$.

Name	$\mu_x(\mu_B)$	$\mu_y(\mu_B)$	$\mu(\mu_B)$
Yb11	3.37(5)	−1.9(1)	3.90(8)
Yb12	−3.37(5)	1.9(1)	3.90(8)
Yb13	−3.37(5)	−1.9(1)	3.90(8)
Yb14	3.37(5)	1.9(1)	3.90(8)
Yb21	0.81(5)	−2.0(1)	2.2(1)
Yb22	−0.81(5)	2.0(1)	2.2(1)
Yb23	−0.81(5)	−2.0(1)	2.2(1)
Yb24	0.81(5)	2.0(1)	2.2(1)

assuming the irreducible representation $\Gamma_4(A_xG_y)$and the resulting magnetic structure is summarized in Table III. Figure 5(a) shows the magnetic component of the powder pattern along with the best refinement, an excellent fit is achieved ($R_p = 0.035$).

The magnetic moments of the two Yb ions are quite different in the a direction but are similar along b. The total ordered moment for the two Yb ions are different: 3.88(8) μ_B for Yb1 and 2.17(10) μ_B for Yb2. They are both reduced from the fully ordered value of $4\mu_B$. Such a reduction in the ordered moment is a feature of compounds with low-dimensional or frustrated interactions and where single-ion anisotropy competes with the magnetic interactions. Figures 5(b) and 5(c) show the magnetic structure of $SrYb_2O_4$. The spins within each chain are collinear, aligning ferromagnetically along the "legs" and antiferromagnetically along the zigzag, while the spins of different chains are canted with respect to each other

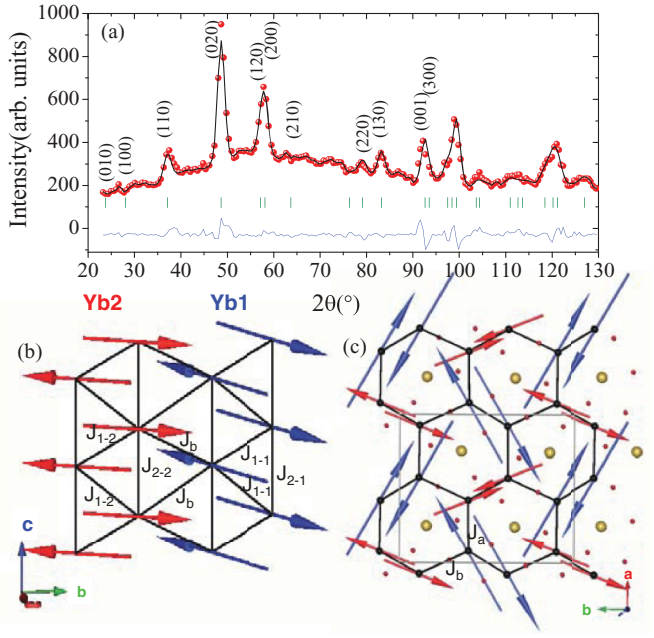

FIG. 5. (Color online) (a) Magnetic powder pattern of $SrYb_2O_4$ collected on D7 at 30 mK. The magnetic structure where the arrows represent the Yb^{3+} ions spins (Yb1 blue, Yb2 red) (b) along the zigzag chains and (c) projected onto the ab plane. The Sr^{2+} and O^{2-} ions are represented by yellow and red circles, respectively.

at angles close to 90°. It is possible to swap the moment's sites, exchanging Yb1 with Yb2 in the refinement but this gives a worse fit, calculating insufficient intensity for some reflections.

The possible inequivalent exchange interactions are also plotted on Figs. 5(b) and 5(c) for comparison with the magnetic order. The Yb1 zigzag chains are built from the zigzag interaction J_{1-1}, and the leg interaction J_{2-1} (for Yb2 these interactions are labeled J_{1-2} and J_{2-2}). The magnetic structure is clearly able to satisfy the J_1-type interactions of both chains but not the J_2 interactions (assuming both are antiferromagnetic). From this, we conclude that the J_1's are much stronger than J_2's ($J_{1-1} > 4J_{2-1}$ and $J_{1-2} > 4J_{2-2}$). The interactions between the zigzag chains (J_a and J_b) are also clearly not satisfied whether they are ferromagnetic or antiferromagnet due the noncollinear spin order at these bonds. This is unexpected because these bonds are not geometrically frustrated (since the moments are aligned parallel along the legs) and either parallel or antiparallel order would be possible. This noncollinearity is therefore due to the single ion anisotropy that must be stronger than J_a and J_b and favors different ordering directions for the Yb1 and Yb2 moments.

D. Low-energy magnetic excitations

Low-energy magnetic excitations have been measured on a single crystal using the ToF spectrometers IRIS and IN5. The IRIS measurement investigated the low-energy magnetic excitation in the $(H,K,0)$ plane at 50 mK whereas the IN5 experiment investigated the dispersion along all reciprocal space directions at three temperatures, in the AFM phase at 70 mK and above the Néel temperature at 1.6 and 20 K. These magnetic excitations arise from interactions between the Yb^{3+} ions. Taking into account the number of magnetic ions per unit cell, a maximum of eight modes are expected although some may be degenerate.

Figure 6 shows color plots of the scattering as a function of wave vector and energy transfer, the colors give the neutron scattering intensity in arbitrary units. The data collected below the magnetic transition show at least two clear modes plus diffuse scattering. There is a strong intensity modulation, especially along the $(0,K,0)$ direction, being most intense near the Γ points. The excitations have a gap of 0.2 meV. In the $(H,0,L)$ plane, only diffuse features are observed. Some of the modes are broader than the instrumental resolution and diffuse magnetic scattering is detected up to 2 meV along all crystallographic directions, specially along the c^* axis. The presence of broad modes and diffuse scattering is typical of antiferromagnets where the magnetic moments are only partially ordered in the ground state. In the paramagnetic phase the modes are not well defined, but diffuse magnetic scattering remains well above the T_N, again indicating the presence of competing interactions.

E. Magnetic phase diagram

A set of heat capacity and magnetocaloric effect measurements as a function of temperature and magnetic field have been performed on $SrYb_2O_4$ in order to map out the phase diagram of this compound. The magnetic field was applied

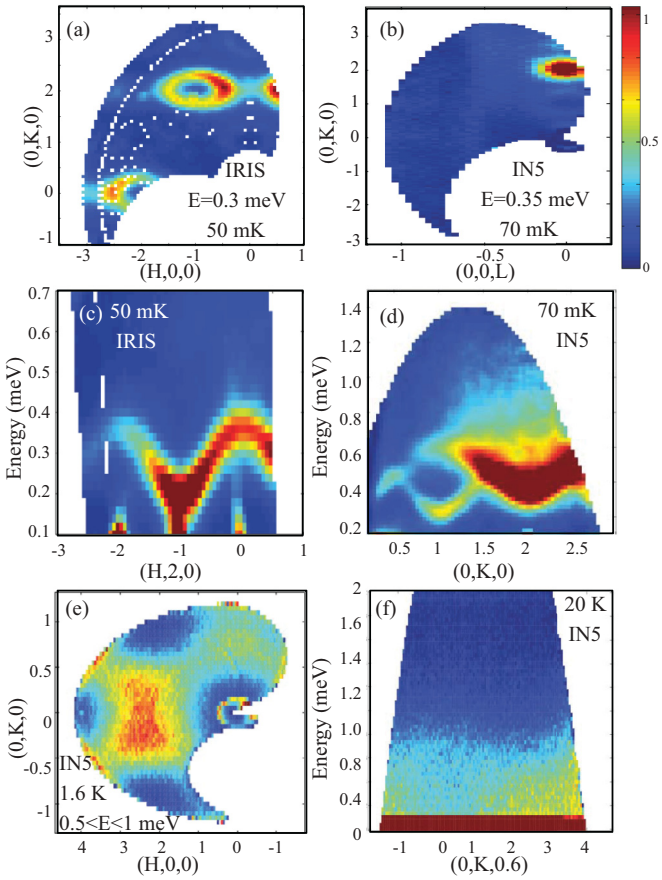

FIG. 6. (Color online) Single-crystal inelastic neutron-scattering data acquired on IRIS-ISIS and IN5-ILL at different temperatures, the color gives the scattered intensity in arbitrary units. (a) and (b) Constant energy color plots showing the $(H,K,0)$ and $(0,K,L)$ plane at $E = 0.3$ and 0.35 meV, both below the Néel temperature, there are minima at $(\pm 2,0,0)$ and $(\pm 1,2,0)$. (c) and (d) E-Q cuts along $(H,2,0)$ and $(0,K,0)$ in the AFM phase, the excitations have a gap of 0.2 meV. (e) Constant energy color plot showing the $(H,K,0)$ plane integrated in the energy range $0.5 < E < 1$ meV at 1.6 K above Néel temperature. (f) Constant cut along $(0,K,0.6)$ at 20 K, diffuse magnetic scattering is intense up to 1 meV.

along the three crystallographic directions for temperatures above and below T_N.

Figure 7(a) shows the adiabatic temperature changes for both increasing and decreasing applied magnetic field along the c axis. At $T = 0.6$ K two transitions are observed, the first one at ≈1.1 T is a second-order transition while the second at ≈4.5 T is broader and could be defined as a crossover. The crossover might be linked to the close proximity in phase space of a critical point that can be reached only by the application of some other external parameter such as pressure. The integral of $(\partial M/\partial T)|_B$ over field gives the entropy variation, this is plotted in Fig. 7(a) in red. For the lower-field transition, there is an abrupt change in the slope of the entropy with field. This suggests a second-order transition from a more ordered state to a less order one, in this case, from the 3D AFM ordered phase to the paramagnetic phase. The higher-field anomaly has smoother entropy change and since the entropy decreases, it

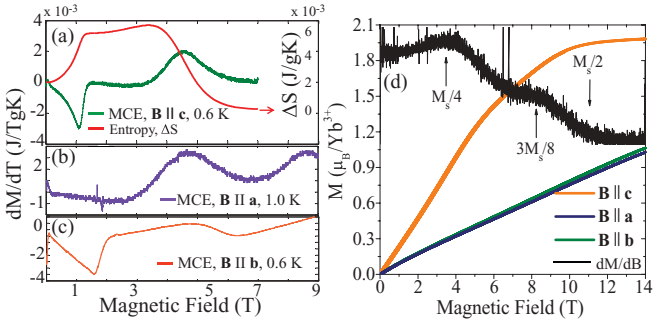

FIG. 7. (Color online) (a) Magnetocaloric effect at 0.6 K for a magnetic field applied along the c axis (green). The relative change in entropy (red line) is overplotted. Magnetocaloric effect at (b) 1 K for a magnetic field applied along the a axis and (c) at 0.6 meV along the b axis. (d) Magnetization as a function of magnetic field applied along the three different crystallographic directions measured at 2 K. The black line is the derivative of the magnetization along the c axis, many crossovers were found.

could be associated with an increase in order, e.g., the magnetic moments start to cant along the field direction.

Along the c axis, two critical fields can be seen below 7 T. For the a axis, the low-field transition is absent but there is a transition at 4.5 T that is similar to the transition found for the c axis. Another crossover happens around 8 T, which also implies a change to a more ordered state [see Fig. 7(b)]. Along the b axis, the features are different, two critical fields at $\approx$1.5 and $\approx$6 T are detected: where the one at lower fields indicates a transition from an ordered state to a less ordered one [see Fig. 7(c)].

Magnetization measurements can also be used to map out the phase diagram. Figure 7(d) shows the magnetization at 2 K along the three crystallographic axes. At 14 T, the magnetic field has not saturated the sample to its full magnetization value of $M_s = g\mu_B J = 4\mu_B$ along any axes. The magnetization for $B \parallel c$ is much greater than for $B \parallel a$ or b at 2 K. The magnetization along c appears to reach a half magnetization plateau of $2.0\mu_B \approx M_s/2$ at a field of $B \approx 11$ T. The magnetization along all directions is highly nonlinear and has multiple crossing points. The derivative of the magnetization along the c axis is shown as a black line in Fig. 7(d), at least three changes in the magnetization slope can be detected. These changes occur at magnetizations of $M_s/4$, $3M_s/8$, and $M_s/2$ and fields of $\approx$4, $\approx$8, and $\approx$11 T, respectively. This is in agreement with the MCE, which shows a crossover point around 4 T. It is expected that these crossovers and transitions will appear sharper in the magnetization at lower temperatures.

Figure 8 shows the phase diagrams as a function of temperature for an applied magnetic field along the three different crystallographic directions. The color scale corresponds to the heat capacity in units of J/K. The colored dots indicate the critical fields extracted from the MCE measurements, which were performed at several temperatures for all three field directions, the triangles are the critical fields extracted from the magnetization measurement. The phase diagram is clearly different along the a, b, and c directions suggesting that the magnetic moments are highly anisotropic. Altogether, Fig. 8 reveals rich and highly complex magnetic behavior. The

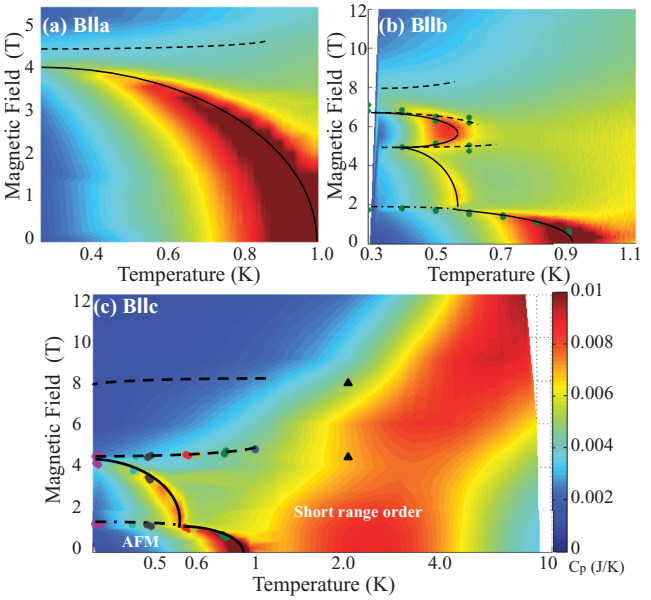

FIG. 8. (Color online) Magnetic phase diagram with magnetic field along (a) a, (b) b, and (c) c axes. The colors indicate the heat capacity in units of J/K. The circles indicate the critical fields extracted from magnetocaloric effect measurements and the the triangles the critical fields extracted from magnetization measurements. Black solid lines show second-order phase transitions. Dash-dot black lines indicate the transition from the AFM phase to a less ordered one. Dashed black lines show metamagnetic crossovers. For the phase diagram along the c axis, above 4.5 T there are just three heat capacity scans at 6, 9, and 12 T, the colors between them result from the interpolation of the data. Below 4.5 T, the data were collected every 0.2 T. The temperature axis is in logarithmic scale.

black solid lines represent the phase boundaries of the second order transitions. Dash-dot black lines show the second order transition from the AFM phase to a less ordered one. Dashed black lines show metamagnetic crossovers.

IV. DISCUSSION AND CONCLUSIONS

An investigation of the nuclear and magnetic structure of the frustrated rare-earth antiferromagnet $SrYb_2O_4$ is presented here, along with single-crystal inelastic neutron-scattering data and the magnetic phase diagram as a function of field and temperature for the three different crystallographic directions. Neutron powder diffraction data were refined in the orthorhombic structure with space group *Pnam* in agreement with previous studies.[17,27–30] No significant changes in the lattice parameters and the atomic positions were found for a large range of temperature.

Heat capacity measurements revealed a magnetic phase transition to long-range magnetic order at $T_N = 0.92$ K. The magnetic structure is antiferromagnetic with ordering wave vector $k = (0,0,0)$. Polarized single-crystal and powder neutron diffraction measurements were performed on D7. A model of the magnetic structure was obtained by the comparison of a simulation of the symmetry analysis results with single crystal polarized diffraction data. The magnetic component of the D7 powder pattern was then refined assuming this model.

Noncollinear order was found with the magnetic moments of both Yb ions lying in the *ab* plane, while the component along the *c* axis is negligible. The two inequivalent Yb^{3+} ions have very different moment sizes and directions. Both moments are reduced from the fully ordered moment of Yb^{3+}, which may be a consequence of the crystal field and/or magnetic frustration. The spins within each zigzag chain are collinear, aligning ferromagnetically along the legs and antiferromagnetically along the zigzag, suggesting that the zigzag interactions (J_{1-1}, and J_{1-2}) are dominant. The spins of different chains are canted with respect to each other at angles close to 90°, suggesting that they point along the anisotropy directions at the expense of the interactions J_a and J_b between the zigzag chains.

The magnetic structure of $SrYb_2O_4$ is different from the magnetic structure of the isostructural compound $SrEr_2O_4$.[18] In that case, the moments point along the *c* axis, and only one of the two Er sites carries a significant magnetic moment. Two types of magnetic order co-exist in $SrEr_2O_4$: one is a fully ordered 3D AFM phase, which appears below a distinct transition temperature, the other is short range order displaying 2D character, with no sharp transition. Hayes *et al.* (see Ref. 32) suggests that only one of the Er ions contributes to each phase and the interaction between the two sites is very small. For $SrDy_2O_4$, no long-range order has been detected down to 20 mK, a 2D short-range ordered phase was observed analogous to that of $SrEr_2O_4$ as well as field induced phase transitions.[19,32]

The low-energy magnetic excitations of $SrYb_2O_4$ were explored by single-crystal inelastic neutron scattering. The excitations extend up to 2 meV and are generally broader than the instrumental resolution. A combination of several gapped modes along with broader diffuse features were observed. The excitations were found to disperse in all crystallographic directions. Above T_N the features become more diffuse but are clearly visible at 1.6 K. Heat capacity measurements showed that the magnetic entropy below 10 K sums up to $R \ln 2$ per Yb, therefore the low-energy magnetic excitations are not due to an excited crystal field level. Instead, they arise from magnetic exchange interactions between the Yb^{3+} ions that create a mean field due to short or long-range order that lifts the degeneracy of the ground-state doublet and gives rise to gapped and dispersive excitations.

Low-energy magnetic excitations have also been observed in the isostructural compound $SrEr_2O_4$ by Hayes *et al.* (see Ref. 32) in which rods of scattering are found in the $(0,K,L)$ plane close to the half integer positions $(0,K,\pm 1/2)$ and $(0,K,\pm 3/2)$ suggesting strong antiferromagnetic correlations along the *c* axis but only weak correlations in the *ab* plane. The diffuse scattering therefore appears to be independent of the magnetic structure that is characterized by $\boldsymbol{k} = (0,0,0)$. Furthermore, the diffuse scattering sharpens only gradually with decreasing temperature and shows no anomaly at T_N.

In $SrEr_2O_4$, the diffuse magnetic scattering is attributed to the Er^{2+} ion that remains paramagnetic.[18] Such behavior indicates cooperative paramagnetism, which is attributed to competing interactions. $SrYb_2O_4$ also shows a large reduction of the ordered Yb^{3+} moments and substantial diffuse scattering below T_N, suggesting competition between the Yb^{3+}-Yb^{3+} interactions and the single-ion anisotropy. The interactions are, however, three dimensional, since the modes disperse in all crystallographic directions in contrast to $SrEr_2O_4$. The nature of the collective magnetic excitations in $SrYb_2O_4$ as well as the higher-energy crystal field levels is currently being studied.

A magnetic phase diagram was also constructed for $SrYb_2O_4$ as a function of magnetic field and temperature using MCE and heat capacity measurements. A large number of transitions and crossovers were found implying a series of metamagnetic phases due to spin-flip and spin-flop processes.[33] Furthermore, the phase diagram was found to be different for fields applied along the *a*, *b*, and *c* directions, suggesting the presence of anisotropy. Metamagnetic behavior is common in highly anisotropic magnetic systems such as $DyPO_4$, $FeCO_3$, $DyAl_5O_{12}$, and CoV_2O_6.[33,34] In $SrYb_2O_4$ it provides further evidence of the competition between interactions and anisotropy.

Altogether these results place $SrYb_2O_4$ alongside the much more extensively studied rare-earth pyrochlores, as insulating magnets where the magnetic interactions compete with each other and with the strong single-ion anisotropy. $SrYb_2O_4$ therefore has the potential to develop exotic phases and excitations as often found in these materials. The results inspire further study. Neutron diffraction experiments are planned in the future to explore the magnetic states revealed by the magnetic phase diagram. In addition, a model of the excitations will be developed to clarify the nature of the competing interactions.

ACKNOWLEDGMENTS

We thank D. M. Le, M. Löwenhaupt, K. Kiefer, K. Prokeš, A. Hoser, S. Maťaš, K. Siemensmeyer, and D. Adroja for helpful discussions.

TABLE IV. Simulated relative intensities of various Bragg peaks for the possible magnetic modes of $SrYb_2O_4$ for the cases when $\mu(\text{Yb1}) = 4\mu_B$, $\mu(\text{Yb2}) = 0$ (upper Table) and $\mu(\text{Yb1}) = \mu(\text{Yb2})$ (lower Table).

$\mu(\text{Yb1}) = 4\mu_B$, $\mu(\text{Yb2}) = 0$									
(h,k,l)	G_x	G_y	G_z	A_x	A_y	A_z	C_x	C_y	C_z
(1,3,0)	2.5	0.7	5	60	9	68	16	2.6	20
(0,2,0)	0	0	0	173	0	73	0	0	0
(0,1,0)	314	0	314	0	0	0.2	0	0	471
(0,3,0)	53	0	53	0	0	0	15	0	15
(1,0,0)	0	0	0	0	126	126	0	437	437
(2,1,0)	4	21	24	12	71	84	6	31	37
(1,1,0)	35	50	85	43	115	198	24	32	56
$\mu(\text{Yb1}) = \mu(\text{Yb2})$									
(h,k,l)	G_x	G_y	G_z	A_x	A_y	A_z	C_x	C_y	C_z
(1,3,0)	0.1	0.1	1	0.1	0.1	0.1	0.1	0.1	0.1
(0,2,0)	0	0	0	690	0	696	0	0	0
(0,1,0)	0.2	0	2	0	0	0	471	0	0.1
(0,3,0)	0.1	0	0.1	0	0	0	0.2	0	0.2
(1,0,0)	0	0	0	0	481	481	0	1769	1770
(2,1,0)	0.1	0.2	0.2	0.1	0.1	0.2	0.1	0.1	0.1
(1,1,0)	0.1	0.2	0.3	0.1	0.1	0.3	1	0.1	0.1

TABLE V. Polarization analysis of specific Bragg peaks performed on D7. The integrated intensity is listed for six polarization channels (**Z**sf, **Z**'nsf, **X**nsf, **X**'sf, **Y**nsf, **Y**'sf). Note that the (**XYZ**) coordinate system used for the polarization (described in the experimental details section) is not the same as (xyz) coordinate system used for the modes or crystal axes. **Z** is the only axis shared by both coordinate systems.

Bragg Peak	Pol.	Integrated Intensity	Remarks
(1,3,0)	**Z** nsf	34.4(6)	strong nuclear
	Z' sf	26.2(5)	magnetic
	Xnsf	51.1(8)	2 Yb ions have different
	X' sf	9.1(2)	moments
	Y nsf	44.5(7)	A_x and/or $A_z \neq 0$
	Y'sf	16.3(3)	
(0,2,0)	**Z** nsf	19(1)	strong nuclear
	Z' sf	31(1)	strong magnetic
	Xnsf	47(2)	A_x and/or $A_z \neq 0$
	X' sf	3.2(3)	
	Ynsf	23(1)	
	Y' sf	26(1)	
(0,1,0)	**Z** nsf	0.0(7)	No nuclear
	Z' sf	0.2(2)	weak magnetic
	Xnsf	0.0(7)	$G_z \approx 0$
	X' sf	0.2(1)	
	Y nsf	0.2(8)	
	Y' sf	0.0(1)	
(0,3,0)	**Z** nsf	0	No nuclear
	Z' sf	0	
	Xnsf	0	$G_x = 0$
	X' sf	0	$G_z = 0$
	Ynsf	0	
	Y' sf	0	
(1,0,0)	**Z** nsf	0.16(5)	nuclear
	Z' sf	0.1(4)	magnetic
	X nsf	0.20(4)	$A_y = 0$
	X' sf	0.13(4)	$A_z = 0$
	Y nsf	0.24(6)	$C_y = 0$
	Y'sf	0.04(3)	$C_z = 0$
(2,1,0)	**Z** nsf	0.000(2)	no nuclear
	Z' sf	2.3(1)	magnetic
	X nsf	2.0(1)	$G_z = 0$
	X' sf	0.45(6)	2 Yb ions have different
	Y nsf	0.48(7)	moments
	Y' sf	1.9(1)	
(1,1,0)	**Z** nsf	0.16(3)	weak nuclear
	Z' sf	9.8(2)	magnetic
	Xnsf	9.7(2)	G_y
	X' sf	0.41(6)	A_x
	Ynsf	0.81(6)	2 Yb ions have different
	Y' sf	9.2(2)	moments

APPENDIX

Representational analysis was performed using the BASIREPS program implemented in the FULLPROF suite.[26] There are two inequivalent Yb^{3+} sites lying at Wyckoff position $4c$, each of which generates four Yb^{3+} ions in the unit cell at fractional coordinates $(x,y,1/4)$, $(-x,-y,3/4)$ and $(x+1/2,-y+1/2,1/4)$, $(-x+1/2,y+1/2,3/4)$. These Yb positions along with the space group *Pnam* and the propagation vector $\boldsymbol{k} = (0,0,0)$ allow four possible types of magnetic order within the ab plane given by the irreducible representations $\Gamma_1(C_xF_y)$, $\Gamma_2(F_xC_y)$, $\Gamma_3(G_xA_y)$, and $\Gamma_4(A_xG_y)$, while along the c axis the ordering follows $\Gamma_5(C_z)$, $\Gamma_6(F_z)$, $\Gamma_7(G_z)$, or $\Gamma_8(A_z)$ (here x, y and z refer to the a, b, c crystallographic directions). It is also possible to have magnetic components along all three crystallographic directions, e.g., the combinations $\Gamma_1 \oplus \Gamma_5$, $\Gamma_2 \oplus \Gamma_6$, $\Gamma_3 \oplus \Gamma_7$, or $\Gamma_4 \oplus \Gamma_8$. The irreducible representations refer to the modes $F(+++)$, $C(++--)$, $G(+--+)$, and $A(+-+-)$, where the symbols in brackets give the relative spin direction (either up "+" or down "−") of the sequence of four Yb ions generated for each Yb site listed above. Since the structure is antiferromagnetic we do not consider the ferromagnetic F mode, which rules out Γ_1, Γ_2, and Γ_6. In order to determine which of the remaining irreducible representations describes best $SrYb_2O_4$, the relative intensities for various Bragg peaks for the x, y, and z components of the A, G, and c modes were simulated using FULLPROF. The results are listed in Table IV. Two cases are considered, first when only one Yb site carries magnetic moment $[\mu(\text{Yb1}) \neq 0, \mu(\text{Yb2}) = 0]$ and the second when the moment on the two Yb sites are equal $[\mu(\text{Yb1}) = \mu(\text{Yb2})]$. Each case produces different Bragg peak intensities.

The results from the representation analysis were compared to the single crystal diffraction data acquired on D7 using **XYZ** linear polarization analysis. The intensities of various peaks in different polarization channels are listed in Table V. Comparison of the magnetic intensities given in the Tables IV and V allows the magnetic structure to be deduced. Table V shows that (1,3,0) has a magnetic component, and this is only possible if the two Yb sites have different magnetic ordered moments as shown in Table IV. The reflection (0,2,0) has strong sf intensities, therefore A_x and/or A_z are present. The (0,1,0) and (0,3,0) reflections are particularly useful, they have no nuclear intensity as revealed by zero counts in some or all of the nsf channels. The modes G_x, G_z, C_x, and C_z are expected to contribute to these peaks and would appear in the **Z**'sf channel. The fact that there is no intensity in this channel proves that those modes are absent. The weak sf intensities of the (1,0,0) peak suggests that the A_y, A_z, C_y, and C_z modes are absent. Therefore the only remaining modes are G_y and A_x: $G(+--+)$, $A(+-+-)$ and the magnetic structure of $SrYb_2O_4$ follows $\Gamma_4(A_xG_y)$.

*diana.quintero_castro@helmholtz-berlin.de

[1]J. Jensen and A. Mackintosh, *Rare-Earth Magnetism* (Clarendon Press, Oxford, 1991).

[2]D. Newman and B. K. C. Ng, *Crystal Field Handbook* (Cambridge University Press, New York, 2000).

[3]K. H. L. Buschow and F. R. de Boer, *Physics of Magnetism and Magnetic Materials* (Kluwer Academic Publishers, New York, 2003).

[4]P. Chandra and P. Coleman, in *Strongly Interacting Fermions and High Temperature Superconductivity: Les Houches Lecture*

Notes (Session LVI), edited by B. Doucot and J. Zinn-Justin (North-Holland, Amsterdam, 1995), pp. 495–594.
[5]L. Balents, Nature (London) **464**, 199 (2010).
[6]S. T. Bramwell and M. J. P. Gingras, Science **294**, 1495 (2001).
[7]J. S. Gardner, M. J. P. Gingras, and J. E. Greedan, Rev. Mod. Phys. **82**, 53 (2010).
[8]A. P. Ramirez, A. Hayashi, R. J. Cava, R. Siddharthan, and B. S. Shastry, Nature (London) **399**, 333 (1999).
[9]S. T. Bramwell *et al*., Phys. Rev. Lett. **87**, 047205 (2001).
[10]J. D. M. Champion *et al*., Phys. Rev. B **68**, 020401 (2003).
[11]L. Savary, K. A. Ross, B. D. Gaulin, J. P. C. Ruff, and L. Balents, arXiv:1204.1320v1 [cond-mat.str-el].
[12]M. E. Zhitomirsky, M. V. Gvozdikova, P. C. W. Holdsworth, and R. Moessner, arXiv:1204.0595 [cond-mat.str-el].
[13]J. S. Gardner, S. R. Dunsiger, B. D. Gaulin, M. J. P. Gingras, J. E. Greedan, R. F. Kiefl, M. D. Lumsden, W. A. MacFarlane, N. P. Raju, J. E. Sonier, I. Swainson, and Z. Tun, Phys. Rev. Lett. **82**, 1012 (1999).
[14]J. S. Gardner, G. Ehlers, N. Rosov, R. W. Erwin, and C. Petrovic, Phys. Rev. B **70**, 180404(R) (2004).
[15]O. A. Petrenko, C. Ritter, M. Yethiraj, and D. McKPaul, Phys. Rev. Lett. **80**, 4570 (1998).
[16]P. P. Deen, O. A. Petrenko, G. Balakrishnan, B. D. Rainford, C. Ritter, L. Capogna, H. Mutka, and T. Fennell, Phys. Rev. B **82**, 174408 (2010).
[17]H. Karunadasa, Q. Huang, B. G. Ueland, J. W. Lynn, P. Schiffer, K. A. Regan, and R. J. Cava, Phys. Rev. B **71**, 144414 (2005).
[18]O. A. Petrenko, G. Balakrishnan, N. R. Wilson, S. deBrion, E. Suard, and L. C. Chapon, Phys. Rev. B **78**, 184410 (2008).
[19]T. J. Hayes, O. Young, G. Balakrishnan, and O. A. Petrenko, J. Phys. Soc. Jpn. **81**, 024708 (2012).
[20]J. R. Stewart, P. P. Deen, K. H. Andersen, H. Schober, J. Barthelemy, J. M. Hillier, A. P. Murani, T. Hayes, and B. Lindenau, J. Appl. Crystallogr. **42**, 69 (2009).
[21]O. Schärpf and H. Capellmann, Phys. Status Solidi **135**, 359 (1993).
[22]O. Schärpf and H. Capellmann, Z. Phys. B **80**, 253 (1990).
[23] http://horace.isis.rl.ac.uk/.
[24] PPMS, User Manual, Quantum Design, San Diego (2004).
[25]K. Kiefer, Ph.D. thesis, Universität des Saarlandes, 2004.
[26]http://www.ill.eu/sites/fullprof/index.html.
[27]J. Pepin, J. Appl. Crystallogr. **14**, 70 (1981).
[28]S. A. Antony, K. Nagaraja, G. Reddy, and O. Sreedharan, Mater. Lett. **51**, 414 (2001).
[29]V. H. Müller-Buschbaum and R. Schenck, Z. Anorg. Allg. Chem. **377**, 70 (1970).
[30]T. Barry and R. Roy, J. Inorg. Nucl. Chem. **29**, 1243 (1976).
[31]E. F. Bertaut, Acta Crystallogr. Sect. A **24**, 217 (1968).
[32]T. J. Hayes, G. Balakrishnan, P. P. Deen, P. Manuel, L. C. Chapon, and O. A. Petrenko, Phys. Rev. B **84**, 174435 (2011).
[33]E. Stryjewski and N. Giordano, Adv. Phys. **26**, 487 (1977).
[34]S. A. J. Kimber, H. Mutka, T. Chatterji, T. Hofmann, P. F. Henry, H. N. Bordallo, D. A. Argyriou, and J. P. Attfield, Phys. Rev. B **84**, 104425 (2011).